Title: Meteorological Drivers of Resource Adequacy Failures in Current and High Renewable Western U.S. Power Systems

Authors:
Srihari Sundar
sriharis@umich.edu, Twitter: @srisun14
Department of Aerospace Engineering, University of Michigan, Ann Arbor, Michigan, USA

Michael T. Craig
mtcraig@umich.edu, Twitter: @TheEnergyCraig
School for Environment and Sustainability, University of Michigan, Ann Arbor, Michigan, USA

Ashley Payne
Tomorrow.io, Boston, MA, USA

David J. Brayshaw
Department of Meteorology, University of Reading, Reading, UK

Flavio Lehner
Department of Earth and Atmospheric Sciences, Cornell University, Ithaca, NY, USA
Climate and Global Dynamics Laboratory, National Center for Atmospheric Research, Boulder, CO, USA

Meteorological Drivers of Resource Adequacy Failures in Current and High Renewable Western U.S. Power Systems

Srihari Sundar[1*], Michael T. Craig[2*], Ashley Payne[3], David J. Brayshaw[4] and Flavio Lehner[5,6]

[1,*]Department of Aerospace Engineering, University of Michigan, Ann Arbor, Michigan, USA.
[2,*]School for Environment and Sustainability, University of Michigan, Ann Arbor, Michigan, USA.
[3]Tomorrow.io, Boston, MA, USA.
[4]Department of Meteorology, University of Reading, Reading, UK.
[5]Department of Earth and Atmospheric Sciences, Cornell University, Ithaca, NY, USA.
[6]Climate and Global Dynamics Laboratory, National Center for Atmospheric Research, Boulder, CO, USA.

*Corresponding author(s). E-mail(s): sriharis@umich.edu; mtcraig@umich.edu;

Abstract

Power system resource adequacy (RA), or its ability to continually balance supply and demand, underpins human and economic health. How meteorology affects RA, particularly with increasing penetrations of renewables, is poorly understood. We characterize large-scale circulation patterns that drive RA failures at increasing wind and solar penetrations by integrating power system and synoptic meteorology methods. At up to 60% renewable penetration and across analyzed weather years, three high pressure patterns drive nearly all RA failures. The highest pressure anomaly is the dominant driver, accounting for 46-100% of risk hours and 57-100% of cumulative risk. The three high pressure patterns exhibit positive surface temperature anomalies, mixed surface solar radiation anomalies, and negative wind speed anomalies across our region, which collectively increase demand and decrease supply.

Our characterized meteorological drivers align with meteorology during the California 2020 rolling blackouts, indicating continued vulnerability of power systems to high pressure anomalies as renewables grow.

Keywords: power system resource adequacy, power system reliability, large-scale circulation patterns, meteorological drivers, Western Electricity Coordinating Council, capacity expansion, self-organizing maps

Access to reliable, or uninterrupted, and low-cost electricity underpins human health, and well-being [1]. Designing a reliable system while minimizing costs is the central objective of power system planning [2]. Reliability partly depends on maintaining resource adequacy (RA), which is the ability to continually balance electricity supply (or generation) and demand despite the occurrence of unexpected events [3]. RA failures are often responsible for large-scale outages (or blackouts), e.g. in California in 2020 [4] and Texas [5] in 2021.

Meteorology affects RA through effects on electricity supply and demand. In bulk power systems dominated by thermal electricity generators, surface air temperature is the main meteorological driver of supply and demand. Low and high surface air temperatures affect demand through increased use of building heating, ventilation, and air conditioning (HVAC) for heating and cooling, respectively [6, 7]. Surface air temperature also affects supply. Specifically, extreme heat increases deratings of thermal power plants [8, 9] and solar photovoltaics, while extreme cold and heat increases forced outage rates of thermal and hydroelectric power plants [10].

Two trends complicate the link between meteorology and RA: (1) increasing penetrations of wind and solar power, and (2) non-stationary meteorology driven by natural variability and anthropogenic climate change. Since wind and solar power are a function of wind speeds and solar irradiance, increasing wind and solar power penetrations will increasingly link electricity supply to these meteorological variables. Wind speeds and solar irradiance exhibit significant spatio-temporal variability [11, 12] and forecast and projection uncertainty [13, 14], complicating RA assessment. Non-stationary meteorology driven by intensifying climate change further complicates RA assessment. As historical meteorology becomes increasingly non-representative of future meteorology, RA assessment will need to increasingly rely on projected future meteorological timeseries to account for the transient nature of the current climate state. However, generating high-quality meteorological projections that account for climate change remains an active area of research limited by methodological uncertainties, and computational power [15]. Generating high-quality future meteorological timeseries is especially challenging at the high spatio-temporal resolution (e.g., hourly) typically required for RA analyses [16].

In response to these challenges, this paper aims to better understand the meteorological drivers of RA and how investment decisions in renewable energy affect those drivers. Better understanding these relationships is crucial for several reasons. First, the meteorology that drives (and co-occurs with) RA failures will determine human health impacts, which can be highly heterogeneous across space and socioeconomic groups [17]. Better understanding the link between decarbonization and drivers of failures can shed light on investment needs in bulk power systems and communities to mitigate possible health impacts and achieve more equitable outcomes. Second, characterization of historic meteorological drivers can guide in evaluating, selecting, and downscaling general circulation models, which is essential for making informed adaptation investments in the power sector [18, 19]. Third, once meteorological drivers of RA failures are characterized, long-range probabilistic forecasting at the subseasonal to seasonal scale can act as a more informed early warning system for system operators and emergency preparedness organizations [20].

We characterize meteorological drivers of RA failures using weather regimes. Weather regimes represent atmospheric circulation as belonging to a finite number of states or patterns [21, 22]. These states are constructed by applying clustering techniques to variables representing large-scale atmospheric flows, e.g., geopotential height. The resulting large-scale patterns have strong associations with surface-level meteorological variables that directly affect the power system, including extreme surface air temperatures [23–25]. The patterns persist over large spatial and temporal scales, and unlike the high-frequency variations exhibited by surface meteorology, the patterns' spatio-temporal variations are better captured by GCMs. Previous research has sought to link the changes in frequency and return periods of these large-scale patterns with the occurrence of extreme events under a changing climate using data from GCMs [26–29].

Our research contributes to two literatures. The first literature analyzes meteorological drivers in the power system, but does not consider RA, a gap that we fill. Within this set, a few studies examine meteorological drivers of periods of low renewable generation or high net demand (demand minus renewable generation) [30–33]. Meteorological drivers in these papers include surface meteorology and atmospheric circulation during these periods. Further, other studies describe weather regimes as drivers of renewable generation, variability, and net demand in the European power system [34–36]. The second literature analyzes RA, but does not consider meteorological drivers, a gap that we also fill. In this broad RA umbrella, studies quantify the effect of using different RA metrics on reserve procurement decisions [37] and capacity values [38]. Other studies quantify the contribution of generators [39, 40] and transmission [41] to RA. A final group of studies quantify system RA under changing generator and/or weather. For instance, Turner et. al. [42] quantify RA changes (in probability and magnitude) driven by decarbonization decisions and climate change impacts on electricity demand and hydropower generation in the Pacific Northwest.

To address these gaps, we answer the following research questions: What large-scale circulation patterns drive regional resource adequacy? And how do these drivers change with increasing wind and solar penetrations? We conduct our study for the U.S. Western Electricity Coordinating Council (WECC) footprint given its rapid growth in wind and solar penetrations, aggressive wind and solar targets, and recent resource adequacy failure [43].

Our analytical pipeline uses methods from power system and synoptic meteorology domains [Figure 1]. We first construct fleets that generate increasing levels of wind and solar electricity (hereafter "renewable electricity" or RE) using a capacity expansion model (CEM) (see Methods.3.2). The CEM is a deterministic linear program that minimizes fixed plus variable costs by determining capacity investments in and/or operations of wind, solar, hydropower, natural gas combined cycle (NGCC), and electricity storage facilities. Investment and operational decisions are subject to numerous constraints, including hourly balance of supply and demand. To capture co-variability and extremes in electricity demand and wind and solar generation, we use observed hourly electricity demand for WECC [44] and coincident RE capacity factors (see Methods.3.5.3). We then quantify a RA profile for each fleet from the CEM using a resource adequacy model (RAM), which simulates stochastic forced outages of generators using a non-sequential Monte Carlo sampling procedure with 10000 samples and finds hours (see Methods.3.3). We use empirically-derived temperature-dependent forced outage rates for NGCC and hydropower facilities and constant outage rates for other generators [10, 45]. The reliability profile output by the RAM identifies hours with a loss of load probability (LOLP) greater than 0.005, which we refer to as "risk hours". Finally, to characterize the meteorological drivers of RA failure, we map the 500hPa geopotential height (Z500) anomalies in these risk hours to the western US extended summer weather regimes. These regimes are constructed based on May - September daily Z500 anomalies from a 40 year period using self organizing maps (SOM), and each regime is represented by a characteristic weather pattern (WP) (see Methods.3.4.1). The characteristic WPs show regimes with varying Z500 anomalies over the region, ranging from positive anomalies (high pressure systems) to negative anomalies (low pressure systems) [Figure 1 "Weather Regimes" panel]. The WPs corresponding to regimes identified based on the risk hours characterize the large-scale patterns contributing to RA failures. By running this integrated modeling framework for four weather years (2016 through 2019) and RE penetrations (13%, 20%, 40%, and 60%), we quantify the effect of increasing renewables on meteorological drivers of RA and the robustness of this effect across weather years. While using four weather years does not necessarily sample the full distribution of possible weather events and associated impacts on RA, it does cover over 35,000 hours and permits us to use observed hourly electricity demand with coincidental wind and solar generation.

1 Results

We divide our results into two sections. First, we quantify the effect of increasing renewable penetrations on meteorological drivers of risk hours for a single

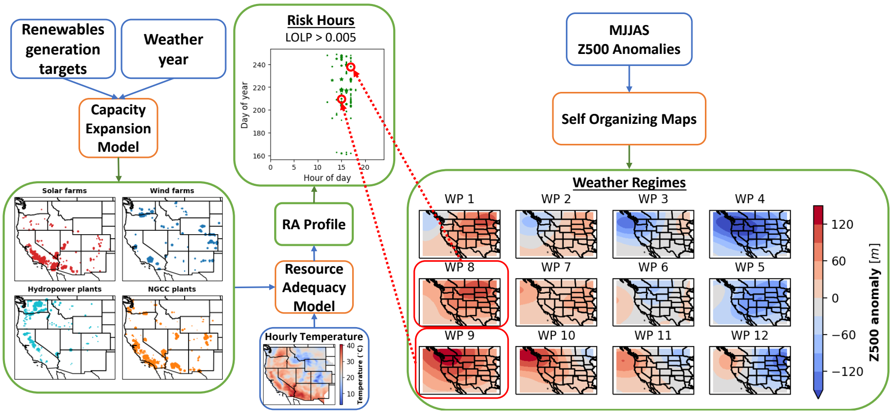

Fig. 1: Our analytical pipeline uses a capacity expansion model (CEM) to construct generator fleets with increasing renewable penetrations and different weather years. Maps show the sizes and locations of facilities for 13% renewables penetration and 2019 weather. These fleets are input into a resource adequacy model (RAM) to quantify hourly loss of load profiles (LOLPs), yielding a resource adequacy (RA) profile. We then map the hours in the RA profile to weather regimes, which we identify with self-organizing maps (SOMs) applied to 500hPa geopotential height (Z500) anomalies. Depicted weather regimes are the SOM outputs for extended summer months, with positive anomalies (high pressure systems) in the bottom-left and negative anomalies (low pressure systems) in the top-right. By varying renewable penetrations and weather years, we characterize meteorological drivers of risk hours (or periods of low RA). Red arrows depicting attribution of risk hours to weather regimes is for illustrative purposes only.

weather year (2019). Second, we repeat this analysis to characterize meteorological drivers of risk hours across multiple weather years at increasing renewable penetrations.

1.1 Meteorological drivers under increasing renewable penetrations for the 2019 weather year

Using our CEM, we construct generator fleets in which RE generation accounts for increasing percentages of annual demand. As renewable penetrations increase from 13% (or current levels) to 60% of annual demand, wind and solar capacities increase from 28 GW to 141 GW and from 22 GW to 112 GW, respectively, while NGCC capacities decrease from 107 GW to 75 GW [Figure 2(A)]. Figure 2(B) depicts each system's RA profile by showing the magnitude of hourly LOLP and timing of risk hours. Across renewable penetrations, all risk hours occur in summer and early fall months (i.e., June through September). Most risk hours occur between 3 and 6 PM Pacific Standard Time (PST), but occur as early and late as 12 and 7 PM PST (UTC-08:00). As renewable penetrations increase from 13% to 60%, the number of risk hours decrease from 68 and 50 and increasingly concentrate into the period between 4 and 6 PM PST. The decrease in risk hours is driven by increasing available generation in many hours of the year, including in hours that previously had low LOLPs. In these hours, increasing available generation results from wind and solar capacity increases exceeding NGCC capacity decreases. As risk hours decrease, hourly LOLPs increase. For instance, as renewable penetrations increase from 13% to 60%, maximum LOLPs increase from 0.17 to 0.26 [Figure SI.8].

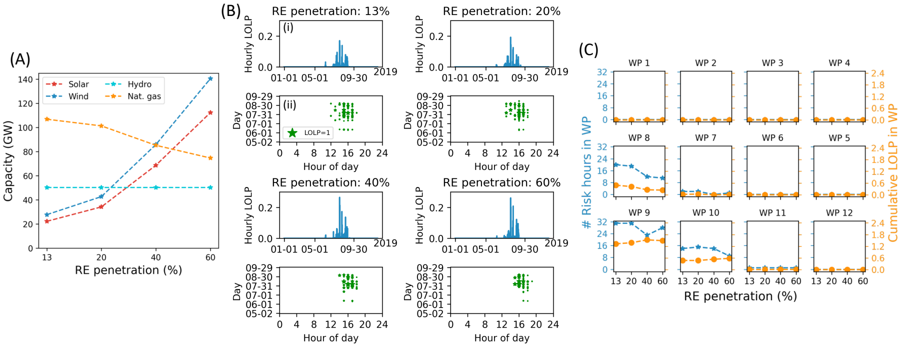

Fig. 2: For the 2019 weather year this Figure SI.hows: (A) Installed capacities of technologies with increasing renewable penetrations. (B) For each renewable penetration, (i) hourly LOLPs across the entire year (i.e., the RA profile) and (ii) the date and hour of day (in PST) when RA failures occur, where the size of star is proportional to the LOLP and the legend shows marker size for LOLP=1. An LOLP of 0.1 indicates demand exceeds available capacity in 10% of the 10,000 simulated hours in the RA model. (C) For each renewable penetration, number of risk hours (blue lines) and cumulative LOLP (orange lines) attributed to each weather regime, where WPs correspond to figure 1.

To attribute RA failures to WPs, we map each risk hour to the prevailing weather regime, then quantify the number of risk hours and cumulative LOLP in each regime [Figure 2(C)]. The cumulative LOLP equals the sum of LOLPs across hours mapped to a given weather regime, so is a function of the number of risk hours in a given weather regime and the LOLP in each of those hours. The cumulative LOLP also equals the expected loss of load hours (LOLH) attributed to each regime. Using either number of risk hours or cumulative LOLP metrics, WPs 8,9, and 10 predominantly drive RA failures across renewable penetrations [Figure 2(C)]. These WPs correspond to high pressure anomalies that cover the entire Western US (as shown in Figure 1). Of those WPs, WP 9 accounts for most RA failures, e.g. 45-56% of risk hours and 57-65% of cumulative LOLP across renewable penetrations. Apart from WPs 8-10, only WPs 7 and 11 account for any RA failures, but these WPs account for less than 3% of risk hours and 1.5% of cumulative LOLP across renewable penetrations.

The relative importance of WPs in driving RA failures is robust across increasing renewable penetrations for the 2019 weather year. As renewable penetrations increase from 13% to 60%, the number of risk hours driven by WP 8 consistently decrease from 20 to 11, respectively, while the numbers of risk hours driven by WPs 9 and 10 exhibit an overall decrease, from 31 to 28 and from 14 to 9, respectively. Increasing renewable penetrations have the opposite effect on cumulative LOLP driven by WPs 9 and 10, indicating increasing LOLPs in risk hours attributed to each WP. As renewable penetrations increase from 13% to 60%, the cumulative LOLPs driven by WPs 9 and 10 increase slightly from 1.3 to 1.5 and from 0.5 to 0.6, respectively [Figure 2(C)]. Conversely, cumulative LOLPs driven by WP 8 decrease from 0.5 to 0.2.

Mechanistically, surface meteorology, not high-pressure anomalies in the middle atmosphere, impact power system RA. To understand how the high pressure anomalies in WPs 8, 9, and 10 drive RA failures, we analyze surface meteorology corresponding to each weather regime [ref. methods 3.4.2]. We find that these WPs correspond to positive surface temperature anomalies, mixed surface solar radiation anomalies, and negative wind speed anomalies across WECC [Figure 3]. Positive temperature anomalies lead to higher generator forced outages and demand. Concurrently, negative solar radiation anomalies lead to lower solar generation. While surface solar radiation anomalies are not negative across WECC, they are largely negative in the Southwest where large amounts of solar capacity are installed [Figure 1]. WPs 8, 9, and 10 also exhibit WECC-wide negative wind speed anomalies, which drive negative anomalies in wind generation. Notably, each of these WPs include surface meteorology anomalies that reduce RA at low and high renewable penetrations, explaining the robustness of these three WPs in driving most RA failures at renewable penetrations ranging from 13% to 60%. Of these three WPs, WP 9 is the largest driver of RA failures across renewable penetrations because it has the largest positive temperature anomaly, largest negative solar anomaly over the Southwest, and largest negative wind speed anomaly over the entire region. Other WPs (i.e., WPs 1-7 and 11-12) do not exhibit the same combination of surface temperature, wind speed, and solar radiation anomalies that WPs 8-10 do, explaining their relative unimportance in driving RA failures.

1.2 Meteorological drivers across different weather years

The above discussion examines drivers of RA failures across renewable penetrations for a single weather year, 2019. Given significant inter-annual variability in meteorology and climate, we repeat our above analysis across four weather years (2016 through 2019) or the duration of our combined data timeseries. This approach treats each meteorological year as an independent observation, allowing us to quantify the robustness of our results to different weather years.

Across weather years and renewable penetrations, solar and wind capacities output by the CEM do not significantly differ across years. For instance,

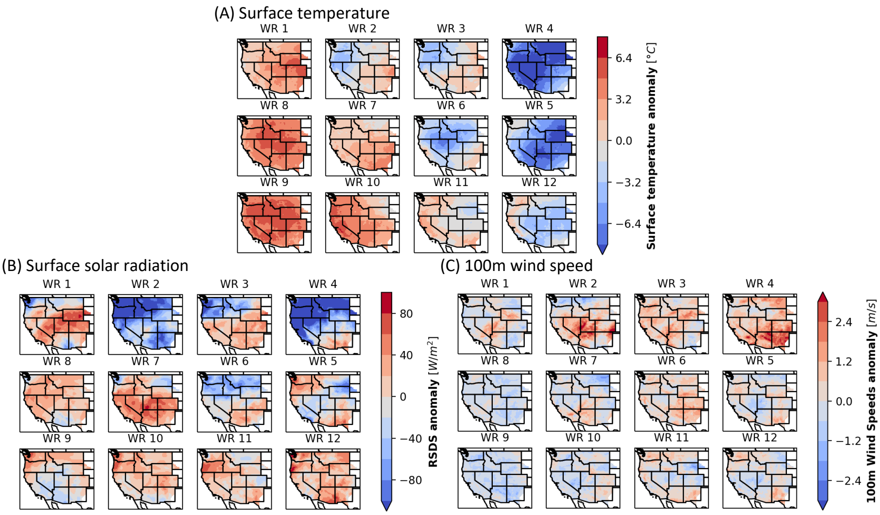

Fig. 3: Composites of surface temperature (A), surface solar radiation (B), and 100 m wind speeds (C) anomalies. The composites are constructed based on the hours from the 2019 extended summer belonging to each weather regime.

at 60% renewable penetration, solar capacities range from 107 to 113 GW, and wind capacities range from 134 to 140 GW across weather years [Figure SI.9(a)]. NGCC capacities exhibit a similar range across weather years, e.g., ranging from 107 to 119 GW at 60% renewable penetration [Figure SI.9(a)]. Our results regarding the number of risk hours and maximum LOLPs are also largely insensitive to different weather years. Specifically, across weather years, risk hours decrease and maximum LOLPs increase with increasing renewable penetrations [Figure SI.9(b)]. For instance, in 2017, risk hours decrease from 47 to 13 and maximum LOLPs decrease from 23% to 62% when renewable penetrations increase from 13% to 60%.

Meteorological drivers of RA failures are also robust to weather years [Figure 4]. WPs 8, 9, and 10, which are all high pressure anomalies, drive most RA failures across all weather years. Collectively, these WPs drive 92% to 100% of all risk hours and 98% to 98% of cumulative LOLP across weather years. Furthermore, WP9 emerges as an even more dominant driver of RA failures in 2016 through 2018 than in 2019. In weather years 2016 through 2018, WP9 accounts for cumulative LOLPs of 2.2 to 2.3 for renewable penetrations of 13% to 40%, relative to 1.3 to 1.5 in 2019 [Figure 4B]. At 60% RE penetrations, WP9 is still the largest driver in all weather years, accounting for 1.5 to 2.35 cumulative LOLP or 64% to 100% of total cumulative LOLP. WP9 occurs more frequently in 2016-2018 than in 2019 [Figure SI.12], which could explain its larger role in driving RA failures than WPs 8 and 10 in 2016-2018 relative to in 2019. The surface meteorology associated with WPs 8-10 in weather years 2016-2018 show similar trends of positive temperature anomalies, negative wind speed anomalies, and negative solar radiation anomalies in the Southwest as in 2019 [see Figures S10-12].

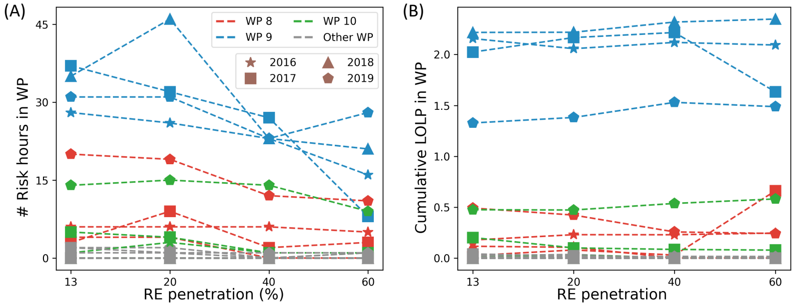

Fig. 4: A - Number of risk hours attributed to each weather regime across the weather years with increasing RE generation levels; B - Cumulative LOLP attributed to each weather regime across the weather years with increasing RE generation levels.

2 Discussion

Maintaining power system RA, and reliability more broadly, faces challenges from evolving supply- and demand-side technologies and non-stationary meteorology. In response to these challenges, this paper characterized meteorological drivers of RA failures by integrating power system and meteorological methods. We found that RA failures in WECC are driven by WPs corresponding to high pressure anomalies (WPs 8,9, and 10 in Figure 1) over the region. These WPs led to high surface air temperatures and low wind speeds across WECC and with low solar irradiance in areas with solar PV facilities. These meteorological conditions caused compounding impacts on electricity supply and demand, ultimately resulting in risk of resource inadequacy (i.e., RA failures). As renewable penetrations increase, the risk of RA failures increasingly concentrates within the WP with the highest pressure anomaly (WP9). Our findings are robust across analyzed weather years (2016 - 2019).

Rolling blackouts in California in the summer of 2020 support our results. On August 14 and 15, the California Independent System Operator (CAISO) instituted rotating electricity outages during an ”extreme heat storm” covering much of the WECC system [4]. These rotating outages were necessitated by higher-than-predicted demand and supply shortages. While we are not able to include 2020 in our analysis due to data limitations, we can analyze atmospheric circulation prevailing during August 14 and 15 using our reanalysis data [Methods 3.5]. We find that the atmospheric circulation on these two days exhibits a high pressure anomaly over the Pacific northwest [Figure SI.13]. This pattern resembles the high pressure WP in our analysis - WP9 - that accounts for most RA failures. Moreover, our SOM identifies the circulation pattern on August 14 and 15 as belonging to WP9. Thus, the California rotating outages provide real-world evidence for the meteorological drivers of RA failures that we identify in our analysis.

While outages threaten human health and well-being regardless of prevailing meteorology, outages during extreme heat can be particularly life threatening [17]. The robustness of high pressure anomalies driving RA failures at renewable penetrations up to 60% suggests that high temperature anomalies will continue to accompany RA failures. Consequences of outages could have disproportionate impacts on vulnerable populations [46], particularly when they align with extreme heat events [47]. Any disparities in outcomes during outages between income groups could widen as upper income individuals increasingly procure distributed energy systems. Our results indicate a long-term need to ensure vulnerable communities have access to potentially lifesaving cooling during outages, e.g., through investing in community hubs at public buildings [48].

Anthropogenic climate change is already affecting weather and climate, including by increasing surface air temperatures across the Western United States [49]. Using the ERA5 reanalysis dataset, we find some evidence for an increase in the frequency of weather regimes with high pressure anomalies from 1981 through 2020 in the extended summer months [Figure SI.14]. During this period, WPs 8, 9, and 10 (high pressure anomalies) occur more frequently, while WPs 1 and 4 (low pressure anomalies) occur less frequently. Increasing and decreasing trends of WPs 4 and 9, respectively, over the last 40 years are statistically significant (p-values less than 0.05) based on a simple linear regression with year as the independent variable and percent of days with the WP as the dependent variable. Specifically, WP9 shows an increase of 0.3 extended summer days per year while WP4 shows a decrease of 0.2 days per year. Given that we found high pressure anomalies, particularly WP9, drive RA failures, their increasingly frequent occurrence might result in more frequent challenges to maintaining RA. More rigorous analyses are needed to discern and attribute WP trends to aspects of the earth system dynamics, including natural variability versus anthropogenic changes. Better understanding how these WPs will evolve under a changing climate [26] would better inform the risk that climate change poses to RA.

Our research offers several opportunities for extensions. First, to capture co-variability between supply and demand, our analysis is limited to four weather years. To capture long-term climate variability, future research could extend our analysis to multi-decadal timespans using historic data from reanalyses or future data from climate models. This expansion faces several challenges, though, including estimating electricity demand and obtaining high resolution climate model outputs. Second, given data and computational tractability limits, our power system models do not capture the role of transmission infrastructure in driving resource adequacy. Accounting for transmission would reveal regional heterogeneity in resource adequacy and meteorological drivers. In neglecting transmission, we also miss the effect of weather patterns on transmission infrastructure, although transmission systems are also vulnerable to high temperature anomalies [50]. Third, in linking specific weather patterns to resource adequacy failures, our research suggests climate downscaling methods designed, trained, and/or validated on these types of weather patterns could be highly valuable in bridging the disconnect between climate and energy system modelling [16]. Additionally, our results suggest RA analyses using future climate data could focus on weather regimes documented here, which could enable a greater computational focus on climate-related uncertainty.

3 Methods

3.1 Area of study

Our area of study is the Western Interconnection, which is the region within the continental United States overseen by the Western Electricity Coordinating Council (WECC). We choose the WECC system for its high existing wind and solar installed capacities, its strong wind and solar resources, its large geographic area which makes it susceptible to large scale meteorology, and its vulnerability to climate change in the near-term. Climate change has already reduced system reliability in WECC, with extreme heat and drought exacerbated by climate change driving outages in California in 2020 [4]. In 2020, WECC demand totaled 724 TWh, with solar and wind generation meeting roughly 6% and 7%, respectively, of demand [51]. We ignore the transmission system within WECC, a common simplification in macro-scale energy system modeling [52, 53], to maintain computational tractability while capturing a full year of hourly meteorology in our CEM.

3.2 Capacity expansion

We use a capacity expansion model (CEM) to project capacity investments across WECC that are needed to meet increasing renewable generation requirements. The CEM is a deterministic linear program that minimizes fixed plus variable costs by deciding investments in and operations of generators while meeting numerous constraints. More specifically, the model decides investment in combined cycle natural gas (NGCC), wind, solar, and storage capacity; hourly generation from NGCC, wind, solar, and hydropower plants; and hourly charging and discharging from storage. Wind and solar capacity investment decisions occur at specific coordinates throughout WECC (see 3.5.3), while natural gas and battery storage capacity investment decisions occur at the interconnection level. We assume that existing hydroelectric capacity remains constant through all the scenarios, no new investment in hydroelectric capacity occurs, and generation decisions occur at the WECC level. We restrict electricity generation to this simplified set of technologies for three reasons. First, coal and other aging generators are rapidly retiring and being replaced by wind, solar, and NGCC [54]. Second, while other types of generating facilities might persist for reasons other than electricity generation, these other types of facilities, e.g. combustion turbines, have similar underlying drivers of outages as NGCCs. Thus, we do not expect substitutions to substantially affect our results. Third, simplifying including generator types allows us to maintain computational tractability while running our CEM across WECC and all hours in a given year.

The CEM includes several system- and generator-level constraints. At the system level, the CEM requires total generation to meet demand in each hour. To approximate system reliability standards, the CEM includes a 15% planning reserve margin, which requires derated capacity to exceed peak demand by at least 15%. Derated capacity accounts for hourly wind and solar generation potential during the peak demand hour, and for scheduled maintenance and unscheduled outages at NGCC and hydropower generators. At the generator level, generation can vary between zero and maximum capacities output by the CEM. Wind and solar generation is also limited by hourly, spatially-specific wind and solar capacity factors (see 3.5.3) while total monthly hydropower generation is limited to historic monthly generation for the modeled weather years (see 3.5). The CEM also includes operational constraints on electricity storage units. These constraints limit each unit's generation to its state of charge in each hour, and track the state of charge over time given charging and discharging decisions. To examine generator fleets with increasing RE penetrations, the CEM requires total RE generation to meet a percent of total annual demand (see section 3.6 for specification of target levels).

In the real-world, wind and solar is deployed as a function of geography, economics, policy, institutions, transmission access, and other factors, some of which are not quantifiable or publicly available. To capture these factors, we constrain our model's installed RE generation sites to current RE locations. Specifically, the CEM's decision variables related to wind and solar capacity investment are two scaling factors. Location-specific wind and solar capacities output from the CEM equal the relevant scaling factor times existing installed wind or solar capacities in each location. This approach maintains the relative distribution of capacity across locations, enhancing real-world insights that can be drawn from our research. In our analyzed scenarios, the CEM also includes a constraint that sets the wind and solar scaling factors to be equal, thereby maintaining the existing ratio between total installed wind and solar capacity. Without this constraint, we find that the CEM indicates only solar investments and no wind investments upto RE penetrations of 40% across all the weather years. Since the CEM optimizes for WECC-wide capacity of NGCC and storage and generation from hydropower, we do not include any location-specific constraints for these assets.

CEM inputs are historical hourly WECC-wide demand data; historical hourly spatially-explicit wind and solar capacity factors; locations and installed capacities for existing solar and wind plants; monthly WECC-wide hydropower generation and installed capacity for existing hydropower plants;

and technology-specific capital and operational costs over our study horizon. We formulate the CEM using the Pyomo optimization package [55, 56] and solve it using CPLEX version 12.6.2. CEM formulation and parameters are detailed in SI.2

After running our CEM across our analyzed renewable penetrations and weather years (see section 3.6), the CEM only invests in storage at a 60% renewable penetration for 2019. This is likely driven by two factors. First, existing hydropower and NGCC investments provide significant flexibility for integrating variable wind and solar, reducing the value of storage. Second, we use 2021 capital costs for 4-hour utility-scale batter storage. Given the lack of investment in storage from our CEM and to facilitate comparison across scenarios, we rerun 2019 at a 60% renewable penetration without storage as an investment option. In future work, we plan to explore how grid-scale storage affects meteorological drivers of RA.

3.3 Resource Adequacy Model

To quantify resource adequacy on an hourly and annual basis, we combine a Monte-Carlo-based non-sequential state sampling procedure with an optimization-based sequential storage dispatch procedure. The state sampling procedure randomly samples forced outages at each generator in each hour of the year 10,000 times via Monte Carlo simulation (see SI.3.1 for justification of sample size). This results in 10,000 independent capacity curves for the year, each of which are paired with observed hourly demand for the year. Forced outages are a function of location-specific ambient air temperatures for NGCCs and hydropower plants[10], are a constant rate of (0.05) for solar and wind plants [45], and are assumed to be zero for storage (see SI.3.2 for forced outage rates used).

For each capacity curve after storage dispatch occurs, we identify a loss of load event as an hour in which hourly demand exceeds available capacity. The hourly loss of load probability (LOLP) equals the probability that demand exceeds available capacity in that hour across all simulations. We refer to any hour with a $LOLP > 0.005$ to be a "risk hour".

Unlike our RAM, our CEM does not account for stochastic outages. Instead, the CEM aims to produce a resource adequate system by enforcing a planning reserve margin. To facilitate resource adequacy comparisons across future systems output by our CEM, our RAM adjusts each generator fleet until its annual resource adequacy achieves a target value. Specifically, the RAM iteratively adds or removes NGCC capacity then calculates annual resource adequacy until the annual loss of load hours ($LOLH = \sum(LOLP)$) is 2.4. This target value reflects the real-world 1-in-10 reliability standard widely adopted by utilities. After each generator fleet is adjusted, the RAM estimates the fleet's hourly and annual resource adequacy.

Inputs to the RAM include installed capacities of solar, wind, hydropower, and NGCC plants from the CEM; hourly hydropower generation from the CEM; hourly surface air temperatures; and forced outage rates. The CEM provides location-specific installed capacities for solar and wind power; WECC-wide installed capacities for NGCCs and storage; and WECC-wide hourly generation from hydropower consistent with each RE penetration level. We do not re-dispatch hydropower in our RAM for two reasons: (1) doing so is computationally intractable and (2) CEM captures the changes in hydropower dispatch which can be expected within each month from the increased wind and solar generation, albeit it does not capture the changes for the whole year [see SI.3.3]. To sample outages from realistically-sized power plants, we disaggregate installed capacities and (in the case of hydropower) generation from the CEM into realistic power plant capacities [see SI.3.4].

3.4 Meteorological analysis

3.4.1 Weather regimes

To characterize meteorological drivers of risk hours, we begin by identifying the weather regimes and corresponding circulation patterns that coincide with risk hours. To identify weather regimes in our study region (WECC), we use self-organizing maps (SOMs), which is an unsupervised neural-network-based clustering technique. Unlike other hierarchical and non-hierarchical clustering techniques, SOMs cluster input data into nodes that form a topological representation in which node proximity indicates their similarity. Previous studies have identified weather regimes with SOMs in other contexts, e.g. to quantify the frequency and persistence of weather regimes associated with heat waves [57] and extreme precipitation events [58] in a warming climate.

We create our SOMs using seasonal anomalies of the daily average 500 hPa geopotential height (Z500) for the extended summer season (May through September, or "MJJAS") from 1981-2020. We analyze an extended summer season because our risk hours occur in June through September, so we focus on the warmest months of the year without narrowly constraining our SOMs to a small subset of months. We use Z500 because it captures synoptic-scale atmospheric processes and their relationship with surface meteorology, is persistent over multiple days, and is widely used for weather typing in the US and Europe [25, 32, 59, 60]. To produce the SOM, we use the MiniSom Python package [61] with the following parameterization: grid shape of 3 rows and 4 columns, a *gaussian* neighborhood function, sigma (i.e., spread of neighborhood function) value of 2, learning rate of 0.1, and 5,000 training iterations. These parameter values provide a concise weather regime representation that balances quantization and topographic error [see SI.4].

3.4.2 Surface meteorology

While daily Z500 anomalies are a meaningful variable for weather regime identification via SOMs, the power system is directly affected not by Z500 but rather by surface meteorological variables. Thus, for each weather regime identified by our SOM, we make composite maps of hourly anomalies in surface temperature, surface solar radiation, and near surface wind speed. To calculate these hourly anomalies, we calculate the MJJAS seasonal hour-of-day mean over the 40 years of surface weather data (yielding 24 mean values), then subtract this seasonal hour-of-day mean from each hourly data point. Using these hourly anomalies, we construct composite maps for every weather year analyzed (2016-2019) in a two step process. First, we map each day from the extended summer months to a weather regime by passing daily Z500 anomaly into the SOM. Second, for every hour of each day that belong to each weather regime, we average the hourly surface meteorology anomalies to get the composite surface meteorological anomalies under each weather regime. For solar radiation anomaly composites, we choose only the daylight hours region wide (6AM to 8PM PST) to avoid biasing the composites towards the hours with very low solar radiation.

3.5 Data Description

3.5.1 Demand data

We get hourly WECC electricity demand from a database of screened and imputed data based on observed demand [44]. Due to limited availability of observed hourly electricity demand, the database provides four full years of WECC demand from 2016 through 2019. Though there are techniques to backcast electricity demand based on meteorological and societal factors, these methods exhibit large errors, particularly in predicting extreme demand values [7, 62]. Since demand extremes are a major factor in RA, we opt for observational rather than backcasted demand values.

3.5.2 ERA5 Reanalysis Data

Given that identification of weather regimes requires long-term (multi-decadal) weather data, we use reanalysis weather data for our analysis. Specifically, we obtain weather data from the ERA5 reanalysis dataset [63]. We choose ERA5 because it provides wind speeds at 100 m above surface at hourly resolution, unlike other reanalyses products [64]. ERA5 is also widely used in power systems and synoptic meteorology research [24, 34, 35]. From ERA5, we specifically obtain near-surface air temperature (t2m); dewpoint temperature (tdps); air pressure (sp); zonal and meridional surface wind speeds (u10 & v10); downward shortwave solar radiation at the surface (ssrd); and zonal and meridional wind speeds at 100m level (u100 & v100). We obtain each data field at hourly temporal resolution and 30 km spatial resolution. See SI for more details.

3.5.3 Capacity Factors

We derive solar capacity factors directly from the surface downwelling shortwave radiation data for a EFG-Polycrystalline silicon photovoltaic module using the formulation described by Jerez et. al. [65] [See SI 1.1]. We calculate wind capacity factors using the formulation described by Karnauskas et. al. [66] and the composite 1.5 MW IEC class III turbine from the System Advisor Model [67] [See SI 1.2]. For more details, see the SI.

3.5.4 Technology and Costs

We obtain 2021 technology-specific capital costs and operational parameters for the CEM from the NREL Annual Technology Baseline (ATB) (SI Table 1)[68]. For NGCC operational costs, which equal fuel costs times heat rate [68] plus variable O&M costs [68], we use 2021 natural gas prices of 3.133 \$/MMBtu and heat rate of 8888.75 Btu/kWh from the U.S. EIA [69]. We use a capital recovery period of 30 years for all technologies with a discount rate of 7%. For grid-scale storage, we model 4-hour battery storage with a round trip efficiency (RTE) of 0.8 and decay rate (DR) of 1.5% per month.

3.6 Scenarios

To capture the effect of increasing renewable penetrations on meteorological drivers of reliability, we run four scenarios of increasing wind plus solar penetrations: 13% (current penetration [51]), 20%, 40%, and 60%. These scenarios are enforced in the CEM by constraining constraining annual wind plus solar generation to equal to a percentage of annual electricity demand. Given significant inter-annual variability in meteorology and climate, we run our modeling framework for each renewable scenario for each year of available electricity demand data (2016 through 2019). This approach treats each meteorological year as an independent observation, allowing us to quantify the robustness of our results to different weather years.

Declarations

The authors have no competing interests to declare. Code and data produced for this analysis will be available at a public repository.

Acknowledgments. The results contain modified Copernicus Climate Change Service information 2020. Neither the European Commission nor ECMWF is responsible for any use that may be made of the Copernicus information or data it contains. SS would like to thank the open source knowledge contributors that furthered this research.

References

[1] Desa, U.N.: Transforming our world: The 2030 agenda for sustainable development (2016)

[2] Pérez-Arriaga, I.J.: Regulation of the Power Sector. Springer, ??? (2014)

[3] North American Electric Reliability Corporation: 2021 Long-Term Reliability Assessment (2021). https://www.nerc.com/pa/RAPA/ra/Pages/default.aspx

[4] CPUC, CAISO, CEC: Root Cause Analysis: Mid-August 2020 Extreme Heat Wave (2021). http://www.caiso.com/Documents/Final-Root-Cause-Analysis-Mid-August-2020-Extreme-Heat-Wave.pdf

[5] Mays, J., Craig, M.T., Kiesling, L., Macey, J.C., Shaffer, B., Shu, H.: Private risk and social resilience in liberalized electricity markets. Joule (2022)

[6] Auffhammer, M., Baylis, P., Hausman, C.H.: Climate change is projected to have severe impacts on the frequency and intensity of peak electricity demand across the united states. Proceedings of the National Academy of Sciences **114**(8), 1886–1891 (2017)

[7] Ralston Fonseca, F., Jaramillo, P., Bergés, M., Severnini, E.: Seasonal effects of climate change on intra-day electricity demand patterns. Climatic Change **154**(3), 435–451 (2019)

[8] Zhai, H., Rubin, E.S., Versteeg, P.L.: Water use at pulverized coal power plants with postcombustion carbon capture and storage. Environmental science & technology **45**(6), 2479–2485 (2011)

[9] Loew, A., Jaramillo, P., Zhai, H., Ali, R., Nijssen, B., Cheng, Y., Klima, K.: Fossil fuel–fired power plant operations under a changing climate. Climatic Change **163**(1), 619–632 (2020)

[10] Murphy, S., Sowell, F., Apt, J.: A time-dependent model of generator failures and recoveries captures correlated events and quantifies temperature dependence. Applied Energy **253**, 113513 (2019)

[11] Kumler, A., Carreño, I.L., Craig, M.T., Hodge, B.M., Cole, W., Brancucci, C.: Inter-annual variability of wind and solar electricity generation and capacity values in Texas. Environ. Res. Lett. **14**(4) (2019). https://doi.org/10.1088/1748-9326/aaf935

[12] Haupt, S.E., Copeland, J., Cheng, W.Y.Y., Zhang, Y., Ammann, C., Sullivan, P.: A method to assess the wind and solar resource and to quantify interannual variability over the United States under current and projected future climate. J. Appl. Meteorol. Climatol. **55**(2), 345–363 (2016). https://doi.org/10.1175/JAMC-D-15-0011.1

[13] Jia, B., Xie, Z., Dai, A., Shi, C., Chen, F.: Evaluation of satellite and reanalysis products of downward surface solar radiation over east asia: Spatial and seasonal variations. Journal of Geophysical Research:

Atmospheres **118**(9), 3431–3446 (2013)

[14] Zhang, J., Hodge, B.-M., Gomez-Lazaro, E., Lovholm, A.L., Berge, E., Miettinen, J., Holttinen, H., Cutululis, N., Litong-Palima, M., Sorensen, P., et al.: Analysis of variability and uncertainty in wind power forecasting: an international comparison. Technical report, National Renewable Energy Lab.(NREL), Golden, CO (United States) (2013)

[15] Kotamarthi, R., Hayhoe, K., Mearns, L.O., Wuebbles, D., Jacobs, J., Jurado, J.: Downscaling Techniques for High-Resolution Climate Projections: From Global Change to Local Impacts. Cambridge University Press, ??? (2021). https://doi.org/10.1017/9781108601269

[16] Craig, M.T., Wohland, J., Stoop, L.P., Kies, A., Pickering, B., Bloomfield, H.C., Browell, J., De Felice, M., Dent, C.J., Deroubaix, A., et al.: Overcoming the disconnect between energy system and climate modeling. Joule (2022)

[17] Stone Jr, B., Mallen, E., Rajput, M., Gronlund, C.J., Broadbent, A.M., Krayenhoff, E.S., Augenbroe, G., O'Neill, M.S., Georgescu, M.: Compound climate and infrastructure events: how electrical grid failure alters heat wave risk. Environmental Science & Technology **55**(10), 6957–6964 (2021)

[18] Goodess, C.M., Palutikof, J.P.: Development of daily rainfall scenarios for southeast spain using a circulation-type approach to downscaling. International Journal of Climatology: A Journal of the Royal Meteorological Society **18**(10), 1051–1083 (1998)

[19] Soares, P.M., Maraun, D., Brands, S., Jury, M., Gutiérrez, J.M., San-Martín, D., Hertig, E., Huth, R., Belušić Vozila, A., Cardoso, R.M., *et al.*: Process-based evaluation of the value perfect predictor experiment of statistical downscaling methods. International Journal of Climatology **39**(9), 3868–3893 (2019)

[20] White, C.J., Domeisen, D.I., Acharya, N., Adefisan, E.A., Anderson, M.L., Aura, S., Balogun, A.A., Bertram, D., Bluhm, S., Brayshaw, D.J., et al.: Advances in the application and utility of subseasonal-to-seasonal predictions. Bulletin of the American Meteorological Society, 1–57 (2021)

[21] Michelangeli, P.-A., Vautard, R., Legras, B.: Weather regimes: Recurrence and quasi stationarity. Journal of the atmospheric sciences **52**(8), 1237–1256 (1995)

[22] Casola, J.H., Wallace, J.M.: Identifying weather regimes in the wintertime 500-hpa geopotential height field for the pacific–north american sector using a limited-contour clustering technique. Journal of applied

meteorology and climatology **46**(10), 1619–1630 (2007)

[23] Adams, R.E., Lee, C.C., Smith, E.T., Sheridan, S.C.: The relationship between atmospheric circulation patterns and extreme temperature events in north america. International Journal of Climatology **41**(1), 92–103 (2021)

[24] Rogers, C.D., Kornhuber, K., Perkins-Kirkpatrick, S.E., Loikith, P.C., Singh, D.: Sixfold increase in historical northern hemisphere concurrent large heatwaves driven by warming and changing atmospheric circulations. Journal of Climate **35**(3), 1063–1078 (2022)

[25] Agel, L., Barlow, M., Skinner, C., Colby, F., Cohen, J.: Four distinct northeast us heat wave circulation patterns and associated mechanisms, trends, and electric usage. npj Climate and Atmospheric Science **4**(1), 1–11 (2021)

[26] Fabiano, F., Meccia, V.L., Davini, P., Ghinassi, P., Corti, S.: A regime view of future atmospheric circulation changes in northern mid-latitudes. Weather and Climate Dynamics **2**(1), 163–180 (2021)

[27] Faranda, D., Vrac, M., Yiou, P., Jézéquel, A., Thao, S.: Changes in Future Synoptic Circulation Patterns: Consequences for Extreme Event Attribution. Geophysical Research Letters **47**(15), 1–9 (2020). https://doi.org/10.1029/2020GL088002

[28] Palipane, E., Grotjahn, R.: Future projections of the large-scale meteorology associated with california heat waves in cmip5 models. Journal of Geophysical Research: Atmospheres **123**(16), 8500–8517 (2018)

[29] Francis, J.A., Skific, N., Vavrus, S.J.: North American Weather Regimes Are Becoming More Persistent: Is Arctic Amplification a Factor? Geophysical Research Letters **45**(20), 11414–11422 (2018). https://doi.org/10.1029/2018GL080252

[30] Bloomfield, H., Suitters, C., Drew, D.: Meteorological drivers of european power system stress. Journal of Renewable Energy **2020** (2020)

[31] Brown, P.T., Farnham, D.J., Caldeira, K.: Meteorology and climatology of historical weekly wind and solar power resource droughts over western north america in era5. SN Applied Sciences **3**(10), 1–12 (2021)

[32] van der Wiel, K., Stoop, L.P., Van Zuijlen, B., Blackport, R., Van den Broek, M., Selten, F.: Meteorological conditions leading to extreme low variable renewable energy production and extreme high energy shortfall. Renewable and Sustainable Energy Reviews **111**, 261–275 (2019)

[33] Brayshaw, D.J., Dent, C., Zachary, S.: Wind generation's contribution to supporting peak electricity demand–meteorological insights. Proceedings of the Institution of Mechanical Engineers, Part O: Journal of Risk and Reliability **226**(1), 44–50 (2012)

[34] van der Wiel, K., Bloomfield, H.C., Lee, R.W., Stoop, L.P., Blackport, R., Screen, J.A., Selten, F.M.: The influence of weather regimes on european renewable energy production and demand. Environmental Research Letters **14**(9), 094010 (2019)

[35] Bloomfield, H.C., Brayshaw, D.J., Charlton-Perez, A.J.: Characterizing the winter meteorological drivers of the european electricity system using targeted circulation types. Meteorological Applications **27**(1), 1858 (2020)

[36] Pickering, B., Grams, C.M., Pfenninger, S.: Sub-national variability of wind power generation in complex terrain and its correlation with large-scale meteorology. Environmental Research Letters **15**(4) (2020). https://doi.org/10.1088/1748-9326/ab70bd

[37] Lueken, R., Apt, J., Sowell, F.: Robust resource adequacy planning in the face of coal retirements. Energy Policy **88**, 371–388 (2016)

[38] Ibanez, E., Milligan, M.: Comparing resource adequacy metrics and their influence on capacity value. In: 2014 International Conference on Probabilistic Methods Applied to Power Systems (PMAPS), pp. 1–6 (2014). IEEE

[39] Bromley-Dulfano, I., Florez, J., Craig, M.T.: Reliability benefits of wide-area renewable energy planning across the western united states. Renewable Energy **179**, 1487–1499 (2021)

[40] Pickering, S., Rostkowski, I., Foley, S., Huebsch, M., Claes, Z., Ticknor, D., McCalley, J., Okullo, J., Heath, B., Figueroa-Acevedo, A.: Power system resource adequacy evaluation under increasing renewables for the midwestern us. In: 2019 North American Power Symposium (NAPS), pp. 1–6 (2019). IEEE

[41] Ibanez, E., Milligan, M.: Impact of transmission on resource adequacy in systems with wind and solar power. In: 2012 IEEE Power and Energy Society General Meeting, pp. 1–5 (2012). IEEE

[42] Turner, S.W.D., Voisin, N., Fazio, J., Hua, D., Jourabchi, M.: Compound climate events transform electrical power shortfall risk in the Pacific Northwest. Nat. Commun. **10**(1) (2019). https://doi.org/10.1038/s41467-018-07894-4

[43] WECC: August 2020 Heatwave Event Analysis Report (2021). https://www.wecc.org/Reliability/August%202020%20Heatwave%20Event%20Report.pdf

[44] Ruggles, T.H., Farnham, D.J., Tong, D., Caldeira, K.: Developing reliable hourly electricity demand data through screening and imputation. Scientific data **7**(1), 1–14 (2020)

[45] Kashefi Kaviani, A., Riahy, G.H., Kouhsari, S.M.: Optimal design of a reliable hydrogen-based stand-alone wind/pv generating system, considering component outages. Renewable Energy **34**(11), 2380–2390 (2009). https://doi.org/10.1016/j.renene.2009.03.020

[46] Busby, J.W., Baker, K., Bazilian, M.D., Gilbert, A.Q., Grubert, E., Rai, V., Rhodes, J.D., Shidore, S., Smith, C.A., Webber, M.E.: Cascading risks: Understanding the 2021 winter blackout in texas. Energy Research & Social Science **77**, 102106 (2021)

[47] Klinenberg, E.: Heat Wave: A Social Autopsy of Disaster in Chicago. University of Chicago press, ??? (2015)

[48] Farthing, A., Craig, M., Reames, T.: Optimizing solar-plus-storage deployment on public buildings for climate, health, resilience, and energy bill benefits. Environmental Science & Technology **55**(18), 12528–12538 (2021)

[49] Vose, R., Easterling, D.R., Kunkel, K., LeGrande, A., Wehner, M.: Temperature changes in the united states. Climate science special report: fourth national climate assessment **1**(GSFC-E-DAA-TN49028) (2017)

[50] Bartos, M., Chester, M., Johnson, N., Gorman, B., Eisenberg, D., Linkov, I., Bates, M.: Impacts of rising air temperatures on electric transmission ampacity and peak electricity load in the united states. Environmental Research Letters **11**(11), 114008 (2016)

[51] WECC: State of the Interconnection (2021). https://www.wecc.org/epubs/StateOfTheInterconnection/Pages/State-of-the-Interconnection.aspx

[52] Deshmukh, R., Phadke, A., Callaway, D.S.: Least-cost targets and avoided fossil fuel capacity in india's pursuit of renewable energy. Proceedings of the National Academy of Sciences **118**(13) (2021)

[53] Shaner, M.R., Davis, S.J., Lewis, N.S., Caldeira, K.: Geophysical constraints on the reliability of solar and wind power in the united states. Energy & Environmental Science **11**(4), 914–925 (2018)

[54] Storrow, B.: And now the really big coal plants begin to close. SCI. AM.(Aug. 16, 2019), https://www. scientific american. com/article/and-now-the-really-big-coal-plants-beginto-close (2019)

[55] Hart, W.E., Watson, J.-P., Woodruff, D.L.: Pyomo: modeling and solving mathematical programs in python. Mathematical Programming Computation **3**(3), 219–260 (2011)

[56] Bynum, M.L., Hackebeil, G.A., Hart, W.E., Laird, C.D., Nicholson, B.L., Siirola, J.D., Watson, J.-P., Woodruff, D.L.: Pyomo–optimization Modeling in Python vol. 67, 3rd edn. Springer, ??? (2021)

[57] Horton, D.E., Johnson, N.C., Singh, D., Swain, D.L., Rajaratnam, B., Diffenbaugh, N.S.: Contribution of changes in atmospheric circulation patterns to extreme temperature trends. Nature **522**(7557), 465–469 (2015)

[58] Loikith, P.C., Lintner, B.R., Sweeney, A.: Characterizing large-scale meteorological patterns and associated temperature and precipitation extremes over the northwestern United States using self-organizing maps. Journal of Climate **30**(8), 2829–2847 (2017). https://doi.org/10.1175/JCLI-D-16-0670.1

[59] Loikith, P.C., Broccoli, A.J.: Characteristics of observed atmospheric circulation patterns associated with temperature extremes over north america. Journal of Climate **25**(20), 7266–7281 (2012)

[60] Cassou, C.: Intraseasonal interaction between the madden–julian oscillation and the north atlantic oscillation. Nature **455**(7212), 523–527 (2008)

[61] Vettigli, G.: MiniSom: minimalistic and NumPy-based implementation of the Self Organizing Map (2018). https://github.com/JustGlowing/minisom/

[62] Ghosh, R.: Data-driven stochastic reliability assessment of the us electricity grid under large penetration of variable renewable energy resources. PhD thesis, Carnegie Mellon University (January 2022). https://doi.org/10.1184/R1/17939732.v1. https://kilthub.cmu.edu/articles/thesis/Data-driven_stochastic_reliability_assessment_of_the_US_electricity_grid_under_large_penetration_of_variable_renewable_energy_resources/17939732

[63] Hersbach, H., Bell, B., Berrisford, P., Biavati, G., Horányi, A., Muñoz Sabater, J., Nicolas, J., Peubey, C., Radu, R., Rozum, I., et al.: Era5 hourly data on single levels from 1979 to present. Copernicus Climate Change Service (C3S) Climate Data Store (CDS) **10** (2018)

[64] Olauson, J.: Era5: The new champion of wind power modelling? Renewable energy **126**, 322–331 (2018)

[65] Jerez, S., Tobin, I., Vautard, R., Montávez, J.P., López-Romero, J.M., Thais, F., Bartok, B., Christensen, O.B., Colette, A., Déqué, M., *et al.*: The impact of climate change on photovoltaic power generation in europe. Nature communications **6**(1), 1–8 (2015)

[66] Karnauskas, K.B., Lundquist, J.K., Zhang, L.: Southward shift of the global wind energy resource under high carbon dioxide emissions. Nature Geoscience **11**(1), 38–43 (2018)

[67] Blair, N., Diorio, N., Freeman, J., Gilman, P., Janzou, S., Neises, T., Wagner, M.: System advisor model (sam) general description (version 2017.9. 5). National Renewable Energy Laboratory Technical Report (2018)

[68] Vimmerstedt, L., Akar, S., Mirletz, B., Stright, D., Augustine, C., Beiter, P., Cohen, S., Cole, W., Duffy, P., Feldman, D., et al.: Annual technology baseline: The 2021 electricity update. Technical report, National Renewable Energy Lab.(NREL), Golden, CO (United States) (2021)

[69] Center, B.P.: Annual energy outlook 2021. Energy Information Administration, Washington, DC (2021)

Supplementary Information for Meteorological Drivers of Resource Adequacy Failures in Current and High Renewable Western U.S. Power Systems

Srihari Sundar*[1], Michael T. Craig†[2], Ashley Payne[3], David J. Brayshaw[4], and Flavio Lehner[5,6]

[1]Department of Aerospace Engineering, University of Michigan, Ann Arbor, Michigan, USA
[2]School for Environment and Sustainability, University of Michigan, Ann Arbor, Michigan, USA
[3]Tomorrow.io, Boston, MA, USA
[4]Department of Meteorology, University of Reading, Reading, UK
[5]Department of Earth and Atmospheric Sciences, Cornell University, Ithaca, NY, USA
[6]Climate and Global Dynamics Laboratory, National Center for Atmospheric Research, Boulder, CO, USA

August 30, 2022

1 Capacity factors

1.1 Solar

We derive hourly solar capacity factors for a EFG-Polycrystalline silicon photovoltaic module as[1]:

$$CF_{pv}^{t} = P_{R}^{t}\frac{RSDS^{t}}{RSDS_{STC}} \tag{1}$$

where $RSDS^t$ hourly represents surface downwelling shortwave flux in air $[Wm^{-2}]$ for which we use the *surface solar radiation downwards* variable from ERA5, and the superscript t indexes the hour. Though the variable is referred with short name *SSRD* in ERA5 datasets, we refer to it as *RSDS* following the CF conventions used in climate model intercomparison projects (CMIP) and in various literature. In ERA5 data, this quantity is captured as hourly energy accumulation with units Jm^{-2} but we need to calculate power derived from solar radiation, so we divide hourly accumulation by $3600s$ to obtain the average power during the hour with units Wm^{-2} [1]. All the metorological variables are discreet in time and space (at the dataset resolution), and the index t is dropped hereafter for conciseness. In eq.1, $RSDS_{STC}$ refers to RSDS at standard test conditions and is equal to $1000Wm^{-2}$, and P_R^t is the hourly performance ratio calculated using

$$P_R = 1 + \gamma[T_{cell} - T_{STC}] \tag{2}$$

$$T_{cell} = c_1 + c_2TAS + c_3RSDS + c_4SWS \tag{3}$$

---

*sriharis@umich.edu

†mtcraig@umich.edu

[1] https://apps.ecmwf.int/codes/grib/param-db/?id=169

where T_{cell} is the PV cell temperature, TAS is surface air temperature (*2m temperature* in ERA5, converted from K to $°C$), and SWS is surface wind speed (calculated from *10m u- and v- components of wind* from ERA5). In eq.2, $\gamma = -0.005°C^{-1}$ and $T_{STC} = 25°C$. In eq.3, $c_1 = 4.3°C$, $c_2 = 0.943$, $c_3 = 0.028°Cm^2W^{-1}$, and $c_4 = -1.528°Csm^{-1}$ [2].

1.2 Wind

We calculate wind capacity factors using the formulation described in [3] for the composite 1.5 MW IEC class III turbine with power curves from the System Advisor Model (SAM) [4] as:

$$CF^t_{wind} = p(W^t_{100}) \tag{4}$$

where p is a function describing the power curve and W^t_{100} is the hourly corrected 100m wind speed. The correction accounts for air density and humidity related effects on the wind turbine performance and is carried out as:

$$W_{100} = W_{100,raw}\left(\frac{\rho_m}{1.225}\right)^{1/3} \tag{5}$$

$$\rho_m = \rho_d\left(\frac{1 + HUSS}{1 + 1.609 \times HUSS}\right) \tag{6}$$

$$\rho_d = \frac{PS}{\boldsymbol{R} \times (TAS + 273.15)} \tag{7}$$

Eq.5 scales the wind speed $W_{100,raw}$ for air density as this affects the force exerted on the turbine blades, where ρ_m is the humidity corrected air density, which is in turn derived from the surface specific humidity ($HUSS$) as shown in eq.6. ρ_d is the dry air density which is derived using the ideal gas law from surface pressure [units-Pa](PS) and surface temperature (TAS) as shown in eq.7, where $\boldsymbol{R} = 287.058Jkg^{-1}K^{-1}$ is the gas constant. $W_{100,raw}$ is calculated from the *100m u- and v- components of wind* from ERA5 data. Since ERA5 doesn't provide $HUSS$, we calculate it as (ref.[5]):

$$HUSS = \frac{0.622 \times VP}{0.01 \times PS - 0.378 \times VP} \tag{8}$$

$$VP = 6.112\ exp\left(\frac{17.67 \times TDPS}{TDPS + 243.5}\right) \tag{9}$$

where VP is the vapor pressure and $TDPS$ is the dewpoint temperature at surface in $°C$(*2m temperature dewpoint temperature* in ERA5, converted from K to $°C$).

Across WECC, few locations have wind speeds suitable for class I and II wind turbines based on the average wind speed over 2015-2020 from the ERA5 data (figure 1).As a result, we estimate wind generation for all locations across WECC assuming a class-III wind turbine. The power curve from SAM is provided as the power output at discrete wind speeds (figure 2), and we convert this into a continuous function through linear interpolation using the interp1d function from the SciPy package [cite]. We include the discrete power curve in this SI.

2 Capacity Expansion Formulation

2.1 Objective

The objective of the capacity expansion model (CEM) is to minimize the sum of annualized capacity investment, fixed operations & management cost cost, and variable operational costs.

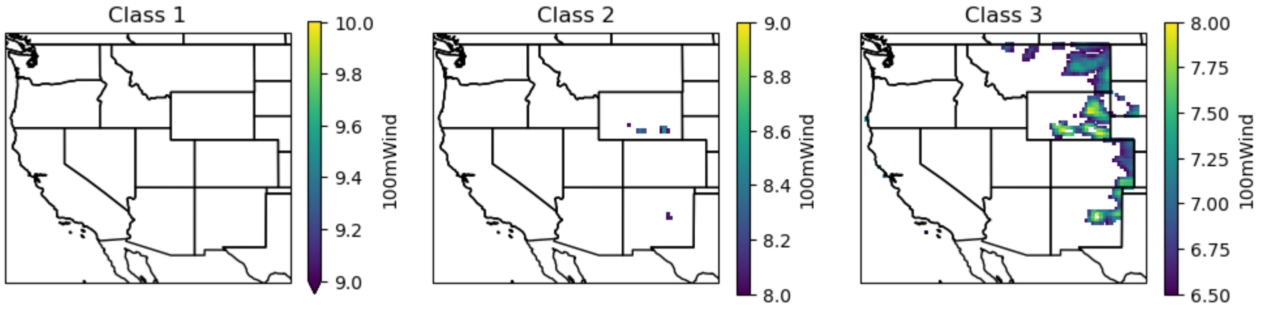

Figure 1: Classification of geographical locations according to wind speed classes, based on 2015-2020 mean of 100m wind speeds

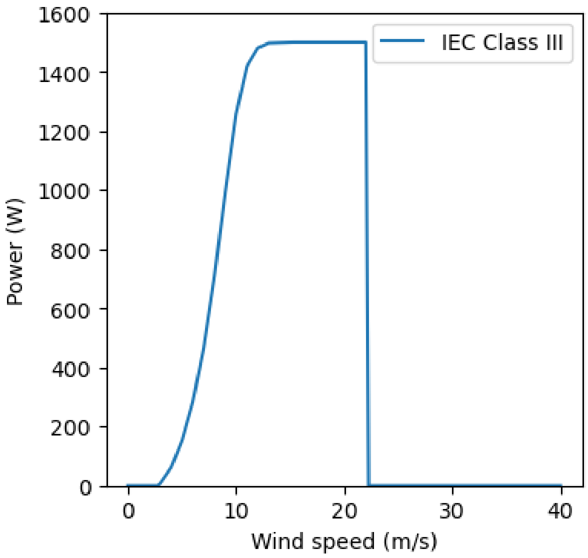

Figure 2: Power curve for 1.5 MW IEC class III turbine

$$\min_{cap_c, gen_c^t} \quad \sum_c [(OCC_c \times CRF_c + FOM_c) \; \times cap_c] + \sum_t \sum_c OC_c \times gen_c^t \qquad \forall\, t \in \mathbb{T},\; c \in \mathbb{C} = \{\mathbb{C}_{re} \cup \mathbb{C}_{hd} \cup \mathbb{C}_{cc} \cup \mathbb{C}_{str}\} \tag{10}$$

where OCC is overnight capital cost of new investments (\$/MW), CRF is capital recovery factor, FOM is fixed operation and maintenance (O&M) costs of units (\$/MW/year), cap_c and gen_c^t are the capacity and hourly generation from generator c which can be solar or wind ($\mathbb{C}_{re}$), hydro ($\mathbb{C}_{hd}$), combined cycle natural gas (CCNG) ($\mathbb{C}_{CC}$), or storage ($\mathbb{C}_{str}$). OC which is the operating cost is defined for new and existing generators as:

$$OC = VOM + HR \times FC, \tag{11}$$

where VOM is variable O&M costs (\$/MWh), HR is heat rate (MMBtu/MWh), and FC is fuel cost (\$/MMBtu). CRF is defined as:

$$CRF = \frac{DR(1+DR)^{LT_c}}{(1+DR)^{LT_c} - 1}, \tag{12}$$

where DR is discount rate and LT is plant lifetime.

2.2 Constraints

2.2.1 Energy balance

This set of constraints ensures that total generation is atleast as much as the demand in every hour of the year.

$$\sum_{c \in \mathbb{C}} gen_c^t \geq D^t, \quad \forall\, t \in \mathbb{T} \tag{13}$$

where D^t is the WECC wide demand in hour t.

2.2.2 Planning reserve margin (PRM)

The PRM constraints are used to ensure that the capacity investments are decided such that the effective generation (accounting for capacity factor for renewables, deratings for non-renewables, and without considering storage contributions) in the hour with the largest demand is at least 15% higher than the demand. This is in line with the PRM followed by system operators and balancing authorities.

$$\sum_{c_{re} \in \mathbb{C}_{re}} [cap_{c_{re}} \times CF_{C_{re}}^{T_{max}}] + \sum_{c_{nre} \in \{\mathbb{C}_{cc} \cup \mathbb{C}_{hd}\}} [cap_{c_{nre}} \times [1 - for_{c_{nre}}(SAT^{T_{max}})]] \geq 1.15 \times D^{T_{max}} \tag{14}$$

where T_{max} is the hour with highest demand in the year, CF is capacity factor, for is the forced outage rate function (ref. section 3.3.2), and SAT is the spatially averaged temperature.

2.2.3 RE capacities

To reflect various factors that drive where wind and solar investments occur, our capacity expansion model controls a variable (k) that scales existing location-specific wind and solar capacity. The scaling variable is a single variable for all wind and solar sites, such that a value of two results in a doubling of installed capacity of wind and solar capacity at each location where they are currently installed. Installed capacity by location is obtained from Form 860 for the year 2020 [6]. From this dataset, each power plant in WECC is assigned to its closest grid point in the ERA5 grid, and the total capacity in each grid point is calculated. So, the resolution at which investment decisions can be made is constrained to the resolution of the ERA5 dataset.

$$cap_{c_{re}} = k \times CAP_{c_{re}}, \qquad \forall\, c_{re} \in \mathbb{C}_{re} \tag{15}$$

where $CAP_{c_{re}}$ is the current installed capacity of solar and wind generators at each grid point.

2.2.4 RE generation

Hourly generation by wind and solar facilities is constrained by hourly capacity factors.

$$\begin{gathered} gen_{c_{re}}^t \leq cap_{c_{re}} \times CF_{c_{re}}^t \ , \\ \forall\, t \in \mathbb{T},\ \forall\, c_{re} \in \mathbb{C}_{re} \end{gathered} \tag{16}$$

$$\tag{17}$$

To test increasing renewable penetrations, we require wind plus solar generation to equal a fraction of annual electricity demand.

$$\sum_{t \in \mathbb{T}} \sum_{c_{re} \in \mathbb{C}_{re}} gen_{c_{re}}^t = REgen \times \sum_t D^t \tag{18}$$

where $REgen$ is the RE penetration level.

2.2.5 Hydropower

Monthly hydropower generation is constrained by a monthly budget aggregated from all hydropower facilities in WECC. This data is obtained form 923 [7].

$$\sum_{t \in T_M, c_{hd} \in \mathbb{C}_{hd}} gen^t_{c_{hd}} = GEN^{T_M}_{hd}, \quad \forall M \in [JAN, DEC] \tag{19}$$

where $GEN^{T_M}_{hd}$ is the observed monthly hydropower generation.

Hydropower generation at each facility also cannot exceed a maximum capacity.

$$gen^t_{c_{hd}} \leq CAP_{c_{hd}}\ , \qquad \forall t \in \mathbb{T}, c_{hd} \in \mathbb{C}_{hd} \tag{20}$$

2.2.6 NGCC

Electricity generation at each NGCC facility cannot exceed the maximum installed capacity.

$$gen^t_{c_{cc}} \leq cap_{c_{hd}}\ , \qquad \forall t \in \mathbb{T}, c_{cc} \in \mathbb{C}_{cc} \tag{21}$$

2.2.7 Storage

This section provides storage constraints. As noted in the main text, our capacity expansion model only invests in storage at a 60% renewable penetration for 2019. Given the lack of investment in storage from our CEM and to facilitate comparison across scenarios, we do not permit our capacity expansion model to invest in storage in generating our results. However, for completeness, we provide the storage constraints here.

Each facility's state of charge varies between time periods based on charging and discharging decisions and the round-trip efficiency penalty.

$$state^t_{c_{str}} = (1-\gamma)\ state^{t-1}_{c_{str}} + \sqrt{RTE}\ charge^t_{c_{str}} - (\sqrt{RTE})^{-1}\ discharge^t_{c_{str}} \tag{22}$$

where γ is the discharge rate per hour, *state*, *charge*, and *discharge* are the hourly energy stored, hourly charging, and hourly discharging respectively of the storage unit and RTE is the round trip efficiency.

The initial state of charge in the first hour of the year at each storage facility equals the full installed energy storage capacity.

$$state^{t=0}_{c_{str}} = EP_{c_{str}} \times cap_{c_{str}} \tag{23}$$

where EP is the energy to power ratio of the storage unit.

State of charge, charging, and discharging variables are bounded between zero and a maximum value (installed power rating for charging and discharging and installed energy capacity for state of charge).

$$0 \leq state^t_{c_{str}} \leq EP_{c_{str}} \times cap_{c_{str}} \tag{24}$$

$$0 \leq charge^t_{c_{str}} \leq cap_{c_{str}} \tag{25}$$

$$0 \leq discharge^t_{c_{str}} \leq cap_{c_{str}} \tag{26}$$

Finally, net generation by each storage facility, which is included in supply and demand balance above, equals discharging minus charging decisions.

$$gen_{c_{str}} = discharge^t_{c_{str}} - charge^t_{c_{str}} \tag{27}$$

2.3 Parameters in CEM

Table 1 shows the costs and parameters used in the CEM.

Table 1: Capital, operational costs, and other parameters for each technology included in our CEM based on the moderate scenario for year 2021 from the 2021 NREL annual technology baseline (ATB)

Generator Type	ATB identifier	Capital Cost \$/MW	Annual Fixed O&M costs \$/MW	Variable costs \$/MWh	Other Details
Solar	Utility-scale solar PV	131,647	22,710	0	-
Wind	Land based wind	134,763	42,263	0	-
Natural Gas Combined Cycle	Average CF NGCC	104,382	27,300	29.59	No CCS
Hydro	-	-	-	0.01	Fixed capacity of 50.228 GW
Storage	Utility-scale battery storage	128,181	32,045	0.01	Energy to power ratio = 4 RTE = 0.8 Discharge rate = 1.5% per month

3 Resource adequacy model

3.1 RAM iteration convergence

Figure 3 provides the LOLH across 50 simulations at varying numbers of Monte Carlo iterations at 13% and 60% renewable penetrations for weather year 2019. As the iteration size increases, the distribution of LOLH estimates tightens. Increasing iterations results in little narrowing of the distribution, but doubles the computation time. To balance accuracy with computational tractability, we run our Monte Carlo simulation for 10,000 iterations.

3.2 Forced outage rate

Table 2 shows the outage probabilities of the various generators as a function of ambient temperature.

Table 2: Temperature dependent forced outage rates of different generators

Closest temperature value $[°C]$	**-15**	**-10**	**-5**	**0**	**5**	**10**	**15**	**20**	**25**	**30**	**35**
NGCC	14.9	8.1	4.8	3.3	2.7	2.5	2.8	3.5	3.5	4.1	7.2
Hydro	7	4.3	3.2	2.7	2.6	2.6	2.7	2.7	2.5	2.9	8.2
Solar, wind	5	5	5	5	5	5	5	5	5	5	5

3.3 Hydro generation

Figure 4 shows annual hydropower generation averaged by hour of day at increasing renewable penetrations for weather year 2019 As renewable penetrations increase, hydropower generation tends to decrease in the middle of the day and increase in the shoulder hours, balancing increasing solar generation midday.

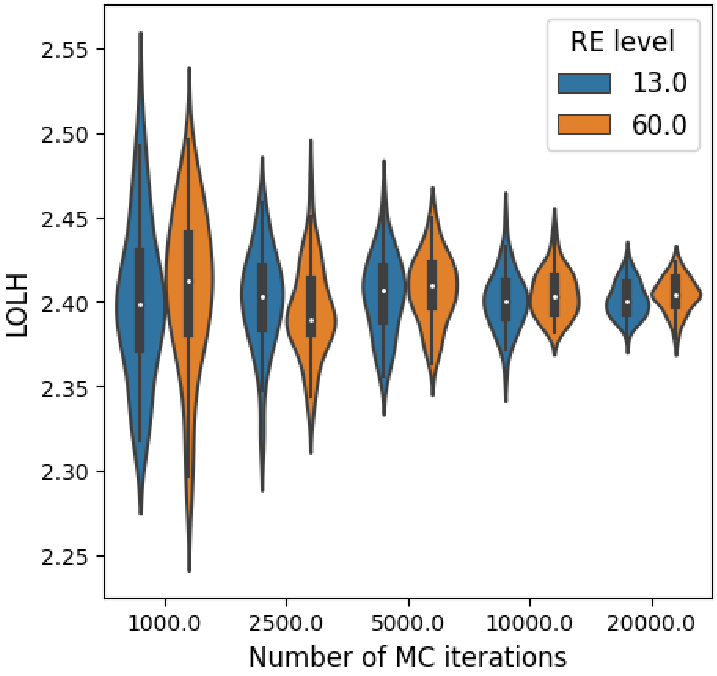

Figure 3: Variation in range of LOLH with increasing number of Monte Carlo samples

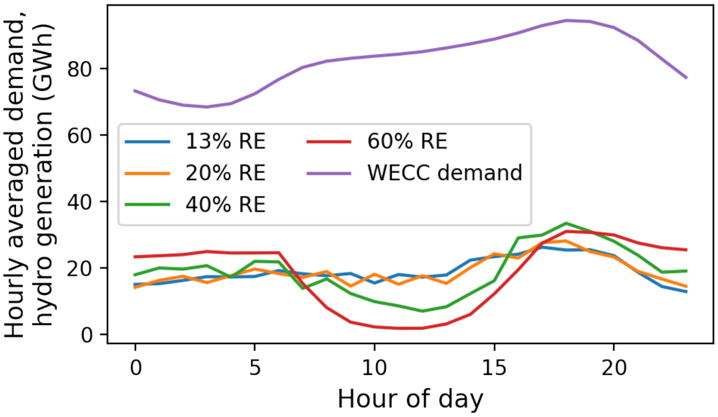

Figure 4: Hourly average hydropower generation and WECC-wide demand from 2019 for different RE penetrations

3.4 Power plant disaggregation

We disaggregate installed solar and wind capacity at each location into plants of up to 26 MW for solar power and 50 MW for wind power. These plant sizes are the median capacities for solar plants (selecting only those with at least 10 MW nameplate capacity to reduce computational costs) and wind plants built in WECC after 2010. Furthermore, to capture spatially-specific temperature-dependent forced outage rates at NGCCs and hydropower plants, we assign WECC-wide NGCC capacity and hydropower generation to specific locations throughout WECC. We spatially disaggregate WECC-wide NGCC capacity by allocating it to locations of existing NGCC locations. For a given location, we set the NGCC capacity equal to the CEM's WECC-wide NGCC capacity times the fraction of existing installed WECC-wide NGCC capacity currently at that location. We then further disaggregate these location-specific NGCC capacities to generators with maximum capacities of 150 MW, which is the median size of NGCC generators built after 2010. For hydropower generation, we perform a similar spatial disaggregation of total capacity to existing locations, and at each location disaggregate plants to generators with maximum capacities of 122 MW, which is the median size of hydropower generators (selecting only those with at least 10 MW nameplate capacity to reduce computational costs) built after 2010. We then disaggregate WECC-wide hourly generation to each location propotional to the fraction of total installed capacity in that location. We implement the RAM in Python and use the Dask library for parallelization [8].

4 Self organizing maps

To test the sensitivity of the SOM technique to grid size and training iterations for identifying weather regimes (WR), we use the metrics quantization error (QE) and topographic error (TE) [9]SI. QE represents the variance within the SOM node and is calculated as the L2 error between the daily circulation maps assigned to a node and the node centroid. TE represents the continuity in the map. TE is calculated by finding the fraction of inputs for which the best matching node (the node it is assigned to) and the second best matching node are not neighboring WRs. So, we want to minimize QE to make the node centroid (weather pattern for our purposes) more representative of the maps assigned to it and minimize TE to ensure the map nodes are topologically continuous. Figure 5a shows how QE and TE vary for different grid shapes used to train the SOM. We find that grid shapes 4x4 and 3x4 (or 4x3) produce maps that balance QE and TE. Figures 6 and 7 show the regimes identified using these two grid shapes. In both cases, the top and bottom rows look very similar. The numbering of the WPs itself is not static as it changes from one training to another, but the relative positions are important. The second from bottom row (WPs 9-12) in the 4x4 map is very similar to the middle row in the 3x4 map. Further, the second row (WPs 5-8) in the 4x4 map is not significantly different from the second from bottom row. As a result, for conciseness we use the 3x4 map. Figure 5b shows the sensitivity of QE and TE to training iterations. We find 5000 iterations to be the optimal number of iterations to minimize both QE and TE, beyond which we over-train the model.

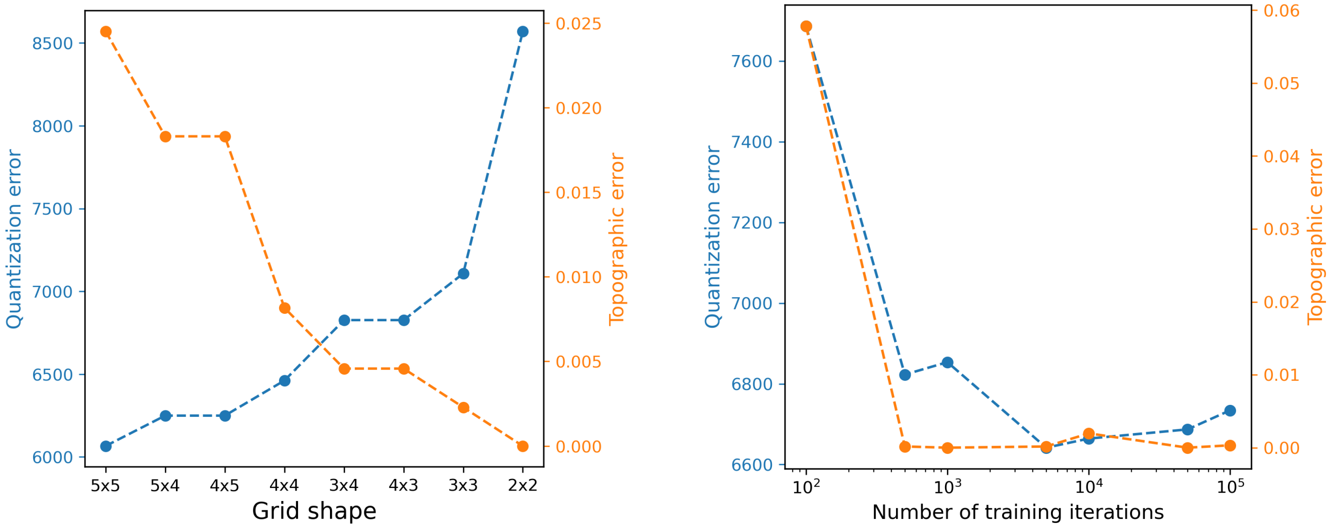

(a)

(b)

Figure 5: Quantization and topographic error for different (a) grid shapes of the SOM (row x columns) (b) training iterations

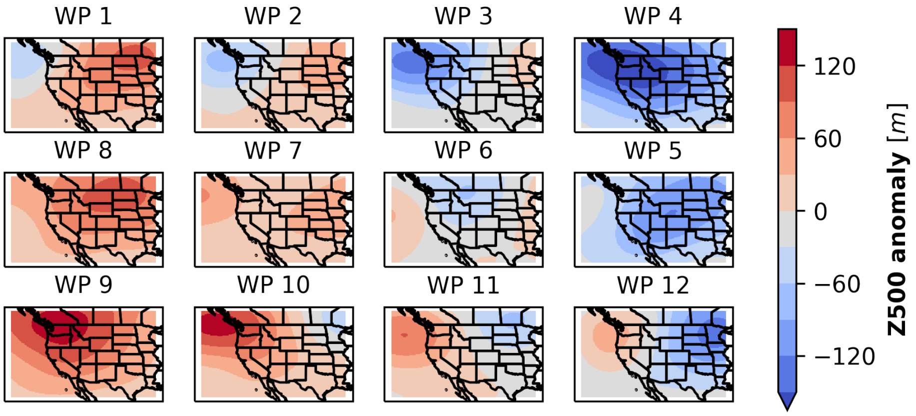

Figure 6: Weather regimes identified using a 3x4 map, replicated from main text

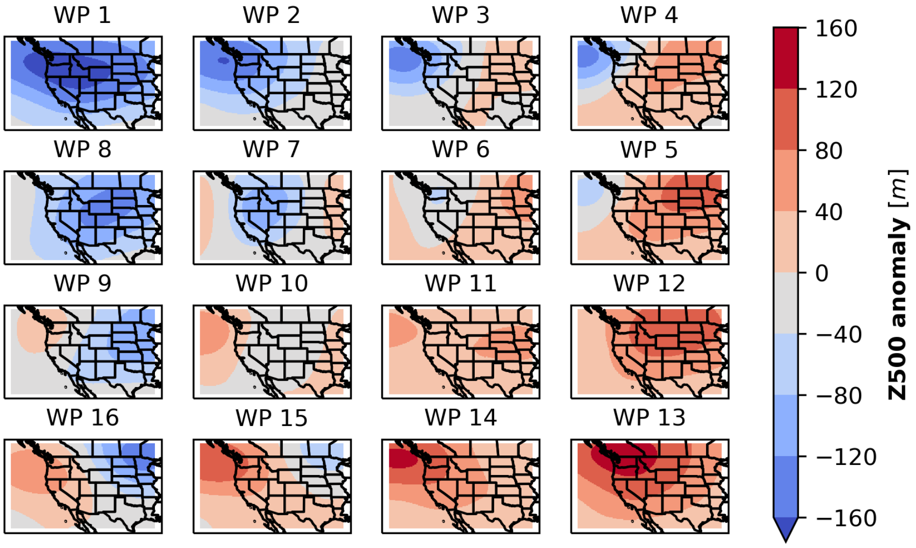

Figure 7: Weather regimes identified using a 4x4 map

5 Results SI

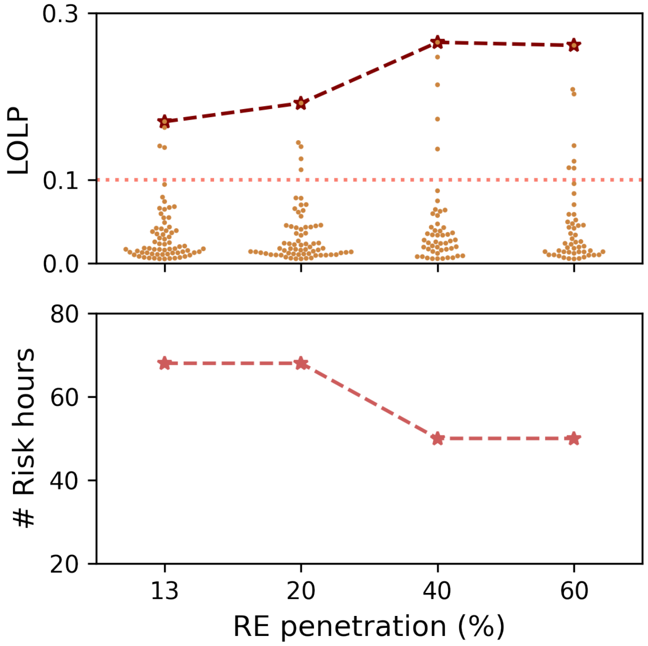

Figure 8: Max LOLP and risk distribution (top panel), number of risk hours (bottom panel) for different RE levels

Figure 9a provides installed capacity across weather years and renewable penetrations. All weather years result in similar generator fleets for each renewable penetration. Hydropower capacity is fixed to existing capacity. The ratio of wind to solar capacity is fixed, as explained in the capacity expansion formulation. Wind and solar capacity vary between 134-140 GW and 107-113 GW at 60% RE penetration, respectively, across weather years. Figure 9b provides the max hourly LOLP and number of risk hours with increasing RE penetration across the different weather years. We see a decrease in the number of risk hours and an increase in max LOLP as RE penetration increases, though these increases and decreases are not monotonic or same across the different weather years.

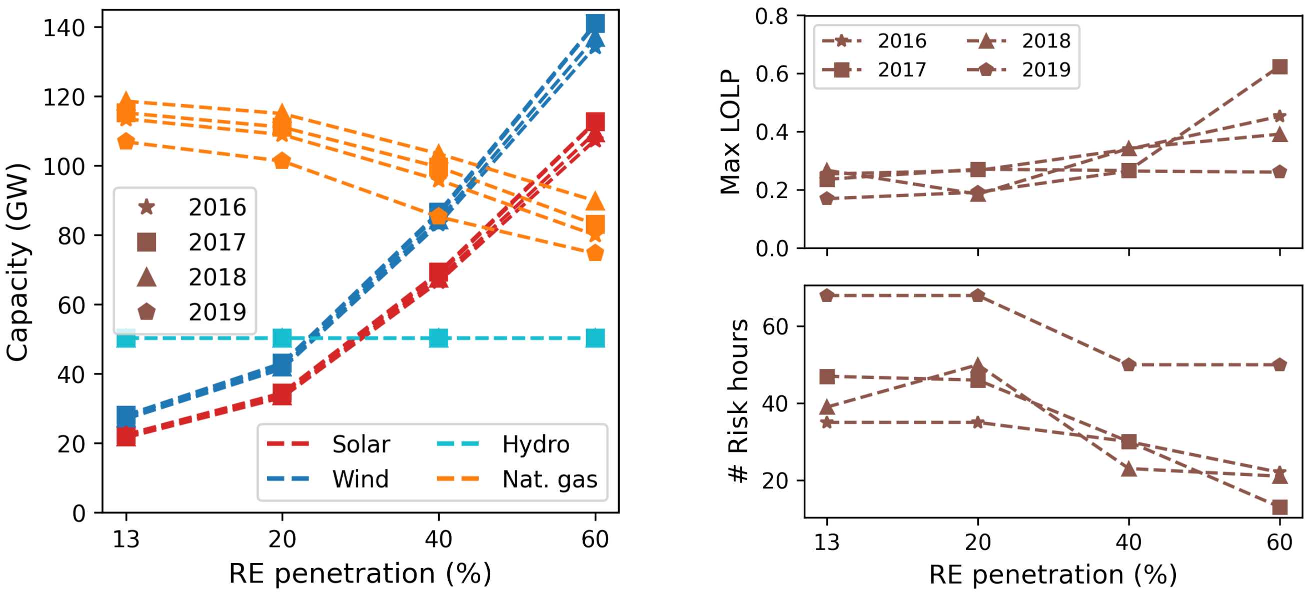

(a)

(b)

Figure 9: (a) Installed capacity of different generation assets across the weather years with increasing RE generation levels; (b) - Max LOLP (top) and number of risk hours (bottom) across the weather years with increasing RE generation levels;

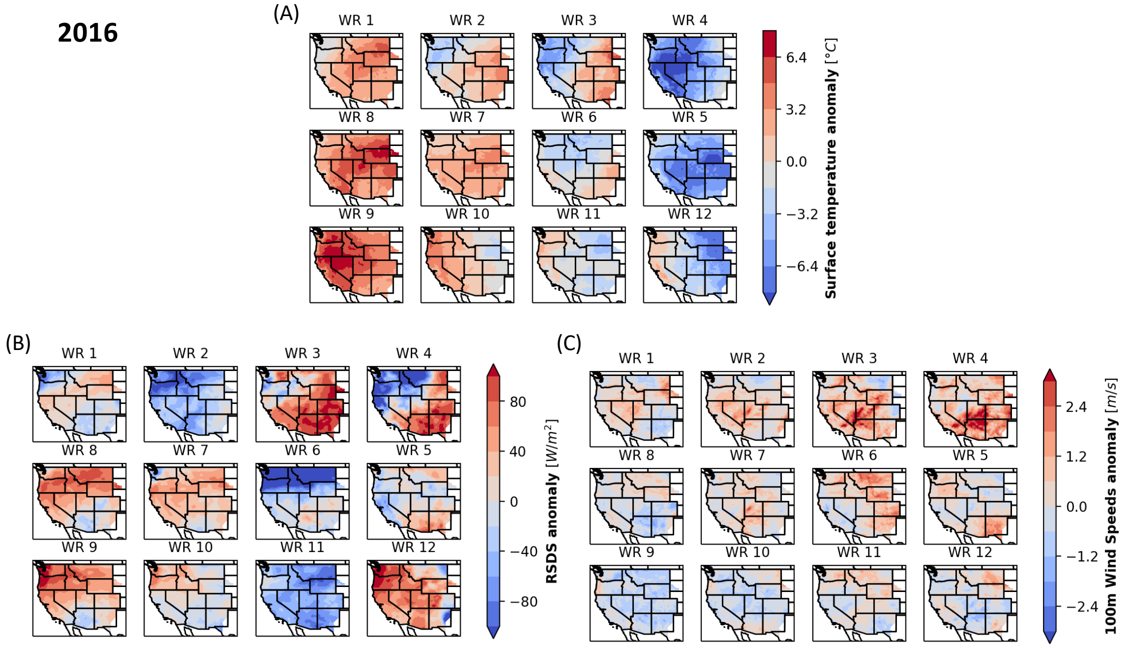

Figure 10: Composites of surface temperature (A), surface solar radiation (B), and 100m wind speeds (C) anomalies. The composites are constructed based on the hours from 2016 extended summer belonging to each weather regime.

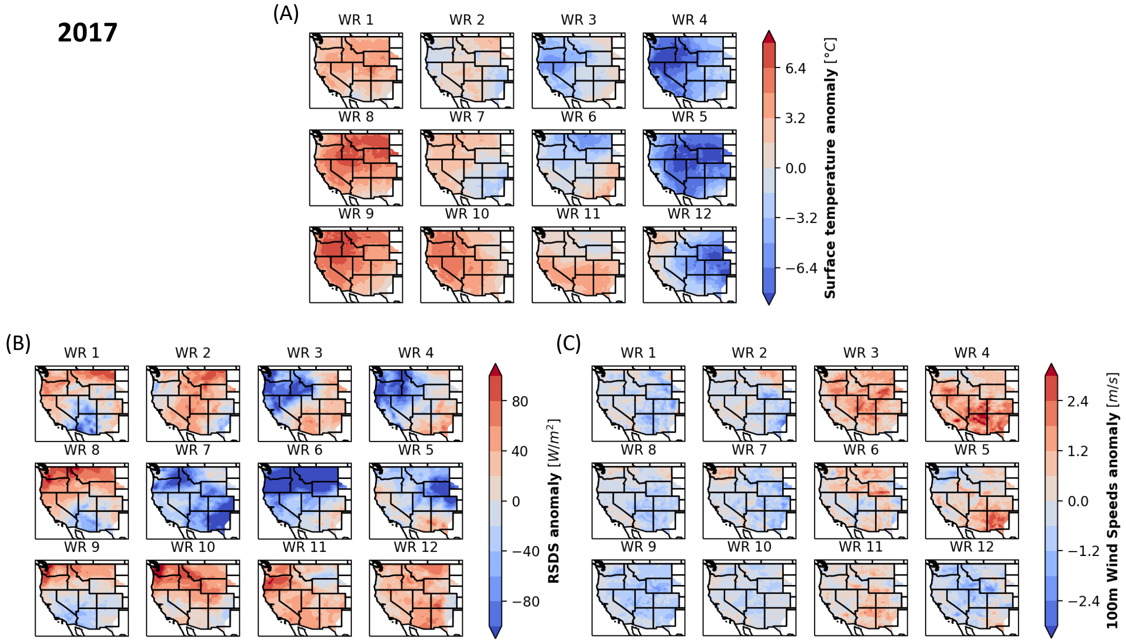

Figure 11: Composites of surface temperature (A), surface solar radiation (B), and 100m wind speeds (C) anomalies. The composites are constructed based on the hours from 2017 extended summer belonging to each weather regime.

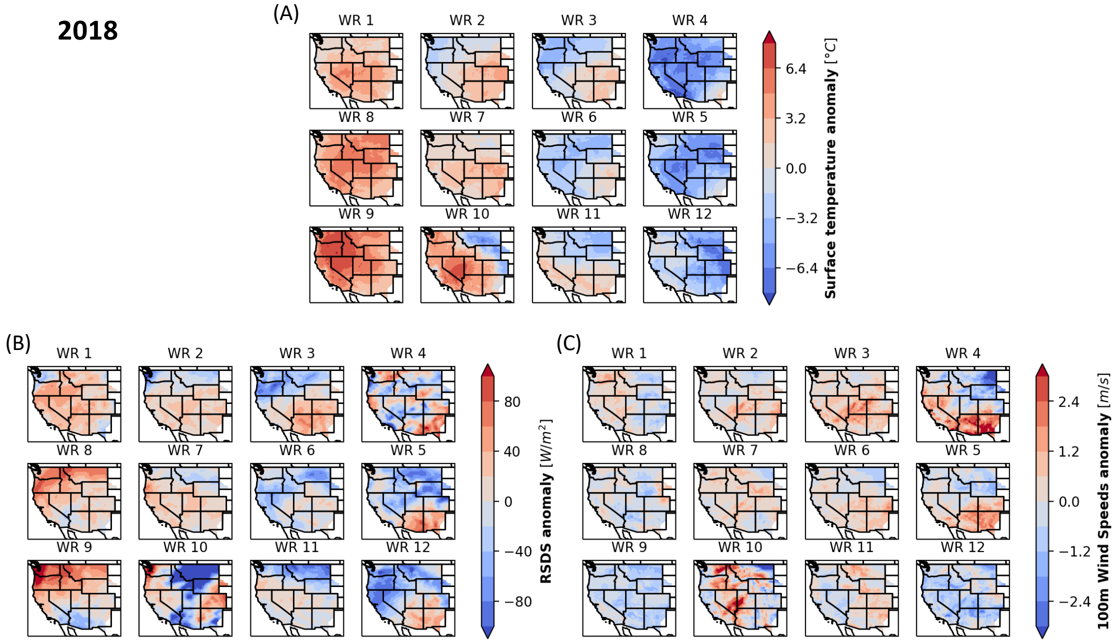

Figure 12: Composites of surface temperature (A), surface solar radiation (B), and 100m wind speeds (C) anomalies. The composites are constructed based on the hours from 2018 extended summer belonging to each weather regime.

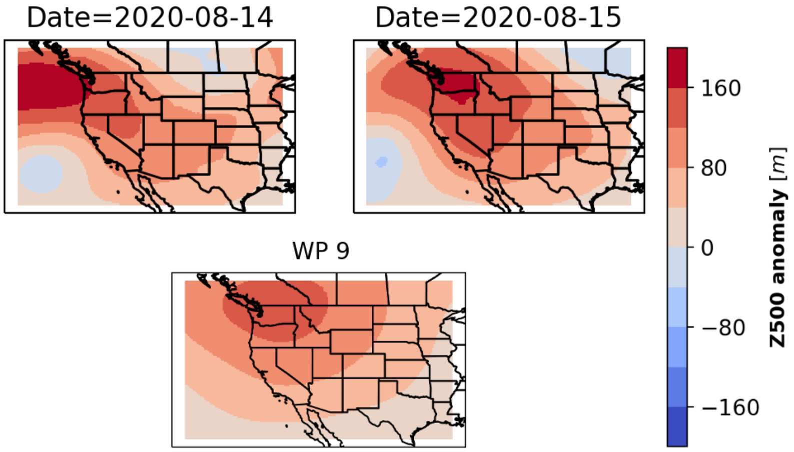

Figure 13: Daily Z500 anomaly on August 14th and 15th 2020 (Top panels) and WP9 from the extended summer weather regimes (Bottom panel). Note the change in color bar range from figure **??**.

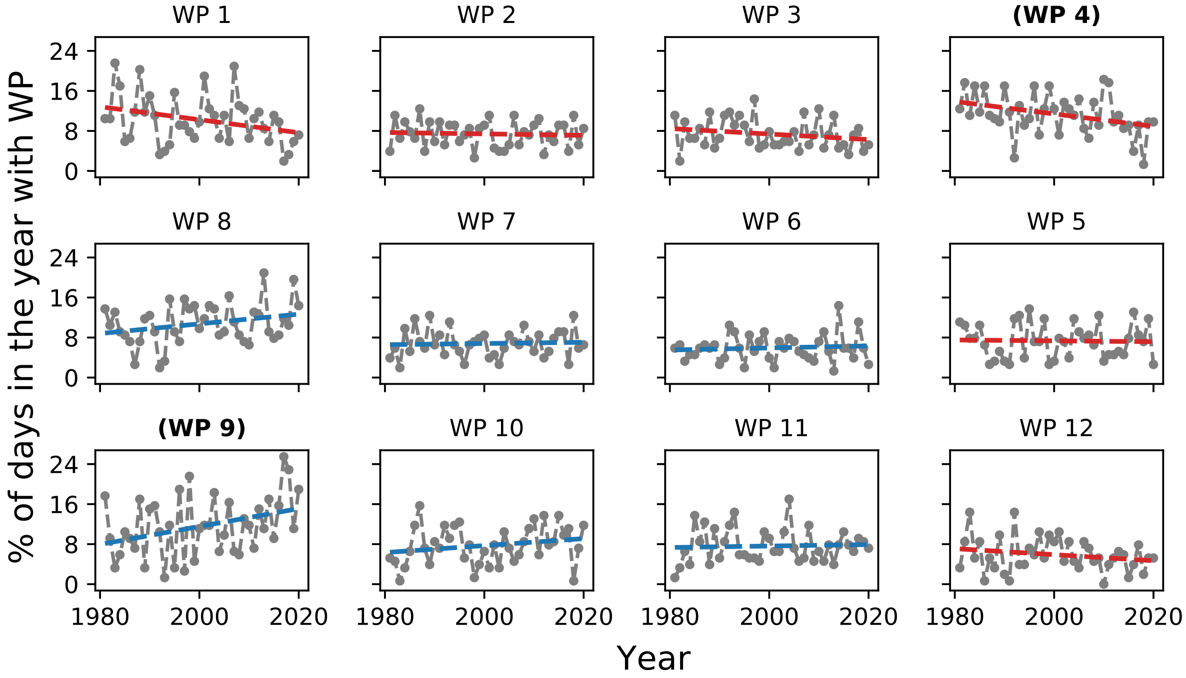

Figure 14: Grey dots show the percentage of extended summer days from 1981 - 2020 belonging to each weather regime. Red (positive slope) and blue (negative slope) dotted lines show a linear regression and bold parenthesized text indicates a 95% statistical significance of regression coefficient.

References

[1] Sonia Jerez, Isabelle Tobin, Robert Vautard, Juan Pedro Montávez, Jose María López-Romero, Françoise Thais, Blanka Bartok, Ole Bøssing Christensen, Augustin Colette, Michel Déqué, et al. The impact of climate change on photovoltaic power generation in europe. *Nature communications*, 6(1):1–8, 2015.

[2] Govindasamy TamizhMani, Liang Ji, Yingtang Tang, Luis Petacci, and Carl Osterwald. Photovoltaic module thermal/wind performance: long-term monitoring and model development for energy rating. In *NCPV and Solar Program Review Meeting Proceedings, 24-26 March 2003, Denver, Colorado (CD-ROM)*, number NREL/CP-520-35645. National Renewable Energy Lab., Golden, CO.(US), 2003.

[3] Kristopher B Karnauskas, Julie K Lundquist, and Lei Zhang. Southward shift of the global wind energy resource under high carbon dioxide emissions. *Nature Geoscience*, 11(1):38–43, 2018.

[4] Nate Blair, Nicholas Diorio, Janine Freeman, Paul Gilman, Steven Janzou, Ty Neises, and Michael Wagner. System advisor model (sam) general description (version 2017.9. 5). *National Renewable Energy Laboratory Technical Report*, 2018.

[5] David Bolton. The computation of equivalent potential temperature. *Monthly weather review*, 108(7):1046–1053, 1980.

[6] Bipartisan Policy Center. Form eia-860 detailed data with previous form data (eia-860a/860b). *Energy Information Administration, Washington, DC*, 2020.

[7] Bipartisan Policy Center. Form eia-923 detailed data with previous form data (eia-906/920). *Energy Information Administration, Washington, DC*, 2016-2019.

[8] Dask Development Team. *Dask: Library for dynamic task scheduling*, 2016.

[9] Cassandra DW Rogers, Kai Kornhuber, Sarah E Perkins-Kirkpatrick, Paul C Loikith, and Deepti Singh. Sixfold increase in historical northern hemisphere concurrent large heatwaves driven by warming and changing atmospheric circulations. *Journal of Climate*, 35(3):1063–1078, 2022.